SAND2008-7112C

Characterizing the Development of Thermal Stratification in an HCCI Engine Using Planar-Imaging Thermometry

John E. Dec and Wontae Hwang*
Sandia National Laboratories

ABSTRACT

A planar temperature imaging diagnostic has been developed and applied to an investigation of naturally occurring thermal stratification in an HCCI engine. Natural thermal stratification is critical for high-load HCCI operation because it slows the combustion heat release; however, little is known about its development or distribution. A tracer-based single-line PLIF imaging technique was selected for its good precision and simplicity. Temperature-map images were derived from the PLIF images, based on the temperature sensitivity of the fluorescence signal of the toluene tracer added to the fuel. A well premixed intake charge assured that variations in fuel/air mixture did not affect the signal. Measurements were made in a single-cylinder optically accessible HCCI research engine (displacement = 0.98 liters) at a typical 1200 rpm operating condition. Since natural thermal stratification develops prior to autoignition, all measurements were made for motored operation. Calibrations were performed in-situ, by varying the intake temperature and pressure over a wide range. Although the absolute accuracy is limited by the pressure-derived temperatures used for calibration, an uncertainty analysis shows that the precision of the diagnostic for determining temperature variations at a given condition is very good.

Application of the diagnostic provided temperature-map images that showed a progressive development of natural thermal stratification in the bulk gas through the latter compression stroke and early expansion strokes. Applying a PDF analysis with corrections for measurement uncertainties provided additional quantitative results. The data show a clear trend of going from virtually no stratification at 305° CA (55° bTDC), to significant inhomogeneities at TDC. Near TDC, the images show distinct hotter and colder pockets with a turbulent structure. Images were also acquired across the charge from the mid-plane to outer boundary layer at 330° CA and TDC. They show an increase in thermal stratification and a change of its structure in the outer boundary layer, and they provide a measure of the boundary-layer thickness. Where possible, results were compared with previous fired-engine and modeling data, and good agreement was found.

INTRODUCTION

The limited high-load capability of homogeneous charge compression-ignition (HCCI) engines is one of the most significant technical barriers to the implementation of this promising technology. HCCI has advantages of high thermal efficiency and very low emissions of NO_X and particulate; however, the maximum load is well below that of spark-ignition (SI) and diesel engines. This load limitation occurs because the cylinder-pressure rise rate (PRR) with combustion increases with increased fueling, eventually becoming so rapid that it results in engine knock.

Previous research has shown that naturally occurring thermal stratification of the charge-gas mixture plays a key role in determining the maximum PRR in HCCI engines [1,2]. For a typical low-residual engine, natural thermal stratification results from wall heat transfer and convection by in-cylinder flows [1]. The resulting thermal inhomogeneities cause the charge to autoignite sequentially starting with the hottest region [1,3], which substantially slows the combustion heat release rate (HRR) compared to a fully homogeneous charge [1]. Moreover, the benefit of a given amount of thermal stratification can be amplified by retarding the combustion phasing [2]. With retarded phasing, the increased expansion rate during combustion increases the induction time of sequentially cooler zones, further slowing the HRR and allowing even higher loads without knock. As a result, the high-load limit of an HCCI engine is closely coupled to the amount of thermal stratification [4], and computational results have shown that increasing the thermal stratifica-

* Currently at General Electric Global Research Center.

The Engineering Meetings Board has approved this paper for publication. It has successfully completed SAE's peer review process under the supervision of the session organizer. This process requires a minimum of three (3) reviews by industry experts.

ISSN 0148-7191

SAE Customer Service: Tel: 877-606-7323 (inside USA and Canada)
Tel: 724-776-4970 (outside USA)
Fax: 724-776-0790
Email: CustomerService@sae.org
SAE Web Address: http://www.sae.org

Printed in USA

SAE International™

tion has a strong potential for extending the high-load limit [2].

Despite the critical importance of thermal stratification to the high-load limits of HCCI, only a little is known about the in-cylinder distribution of the thermal inhomogeneities and how they develop. Chemiluminescence imaging of HCCI combustion has provided evidence of the thermal stratification by showing that even for a well-premixed fuel/air charge, autoignition begins in localized regions located randomly throughout the combustion chamber. High-speed chemiluminescence image sequences then show the remaining charge autoigniting sequentially as a result of the thermal stratification [1,3]. Another key finding from chemiluminescence imaging is that thermal stratification extends throughout the bulk gas rather than being confined to the boundary layer [1]. Moreover, it is this bulk-gas stratification that is mainly responsible for reducing the maximum PRR to allow higher loads, while boundary-layer stratification has only a secondary effect, as discussed in detail in the next section.

Although these chemiluminescence imaging studies provide valuable information on the effect of thermal stratification on the combustion process, they provide no information about the thermal stratification itself. Specifically, they do not show the magnitude of the thermal stratification, its spatial distribution within the bulk gas and boundary layer, or how this stratification develops through the cycle. Understanding these aspects of the thermal stratification is a key step toward developing methods of enhancing it to extend the high-load limit of HCCI.

Planar temperature-map images offer the best means of gaining this desired understanding of the natural thermal stratification. However, previous investigations involving planar imaging of the in-cylinder temperature distribution have been directed at other concerns. Initial work by Einecke *et al.* [5] involved single-shot planar imaging of the end gas temperature in a two-stroke SI engine using two-line excitation of 3-pentanone as a dopant in the fuel. Later, Fujikawa *et al.* [6] used multi-shot averaged two-line excitation of toluene (dopant) in an SI engine to measure thermal distributions resulting both from fuel stratification and from dual-temperature intake streams. A different approach by Kakuho *et al.* [7] involved using a single laser to excite two different dopants (3-pentanone and triethyl-amine) to obtain temperature distributions in an HCCI engine resulting from dual-temperature intake streams. Finally, Rothamer *et al.* [8] obtained simultaneous single-shot temperature-maps and EGR distributions in an HCCI engine using two-line excitation of 3-pentanone as a fuel dopant.

The objective of the current study is to develop an appropriate planar temperature diagnostic and to apply it to an investigation of the development of natural thermal stratification in an HCCI engine. For these measurements, the main purpose is to determine the magnitude and distribution of the temperature inhomogeneities across the charge. Therefore, in selecting a diagnostic, an emphasis was placed on obtaining high precision in measuring the relative temperature variation within an image rather than high absolute accuracy. The technique selected is single-line planar laser-induced fluorescence (PLIF) of toluene as a trace dopant in the fuel (iso-octane). This technique provides sufficient signal to minimize shot noise, and the signal is sufficiently sensitive to temperature variations in the range of interest. It is also straightforward and inexpensive compared to two-laser techniques.

The principle of this diagnostic is based on the temperature sensitivity of the toluene-PLIF signal produced by excitation with a frequency-quadrupled Nd:YAG laser at 266 nm [9,10]. Since variations in fuel/air mixture can also affect the toluene-PLIF signal intensity, the charge was fully premixed. In addition, the intake air was replaced with nitrogen to minimize quenching of the toluene-PLIF signal, and to prevent combustion reactions from breaking down the toluene dopant, which would affect the signal. The absence of combustion is considered acceptable since the focus of this work is to investigate the development of the thermal stratification prior to autoignition. A complete discussion of the diagnostic, including the calibration technique and error analysis, is given in the Experimental Setup and Diagnostics section.

This planar temperature diagnostic was then applied to an investigation of the development of thermal stratification at a typical HCCI high-load operating condition. The results are presented in three parts, following the Diagnostics section. First, temperature-map (T-map) images show the evolution of the thermal stratification in the bulk gases through the latter compression and early expansion strokes. Second, the trends in these images are quantified using a PDF (probability density function) analysis. Third, T-map images of the thermal boundary layer at two representative crankangles are presented and discussed. After presentation of the results, the findings are summarized and conclusions are drawn in the final section.

BACKGROUND

As discussed in the introduction, chemiluminescence imaging has provided considerable information on the effects of thermal stratification on HCCI combustion. Because these findings are related to the motivation and approach for the current study, some key results are briefly reviewed in this section.

In a recent work [1], the authors used chemiluminescence imaging from two different views to determine the progress of combustion in an optically accessible HCCI engine, as shown in Fig. 1. Selected images from these two views are presented in Fig. 2, for a well-premixed operating condition. Figure 2a presents three representative images showing the progress through the combustion event from the bottom view. For this operating condition, the peak HRR and 50%-burn point (CA50) occur at 368° crankangle (CA),[1] as shown in Fig. 3. Even though the charge was well premixed, the combustion is

[1] 0° CA is taken to be top dead center (TDC) intake.

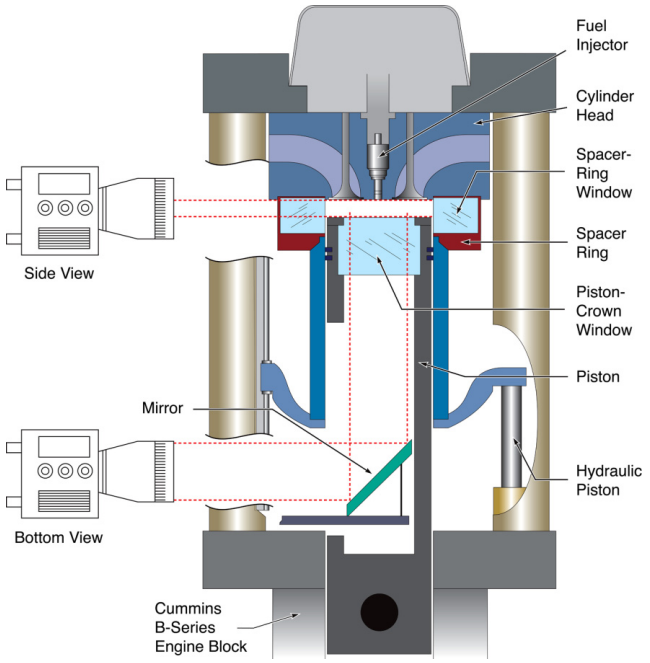

Figure 1. Schematic of optically accessible HCCI engine showing the two different views used for chemiluminescence imaging in Ref. [1].

heterogeneous due to naturally occurring thermal stratification. Early in the combustion event (365° CA), the combustion reactions are underway in localized regions, presumably corresponding to regions of higher temperature. Other regions are still dark indicating that they have not yet autoignited, presumably because they are cooler. These cooler regions sequentially autoignite [1], and by CA50 (368° CA), most regions are reacting intensely. Late in the combustion event (372° CA), the chemiluminescence is weaker (as noted by the higher gain number in white) and spatially more intermittent.

Although the non-uniformities in the bottom-view images in Fig. 2a show the effects of thermal stratification, the role of the thermal boundary layers is not readily apparent. As shown in Ref. [1], for typical engines, thermal stratification results mainly from wall heat transfer. As a result, thermal boundary layers might be considered to play a major role in contributing to the sequential autoignition that controls the maximum PRR. However, the side-view chemiluminescence images in Fig. 2b show that this is not the case. (In the following discussion, it should be noted that the side-view chemiluminescence intensity tracks the HRR well during the main combustion event as shown in Fig. 3.) As evident in the 364° CA image, hot ignition begins in localized regions in the central part (in the vertical direction) of the charge. From 364 - 368° CA, the number of regions showing hot ignition increases rapidly, although inhomogeneities remain, as evident in the bottom view (Fig. 2a). Up past the time of the peak HRR (368° CA, see Fig. 3), hot ignition and combustion occur in the central part of the charge, *i.e.* the bulk gases [1]. There is no indication of any preferential boundary-layer combustion until 370° CA. Then, by 372° CA, the boundary layer combustion along the firedeck (*i.e.*, the flat cylinder-head surface) and piston-top surfaces becomes distinct, while the chemiluminescence in the central region dies out. Based on this, the weaker more intermittent chemiluminescence in the bottom-view image at 372° CA is mainly due to boundary-layer combustion. These findings on the timing of the bulk-gas and boundary-layer combustion relative to the PRR are even more evident in plots of the chemiluminescence-intensity profile from the fire-deck to the piston top averaged over many engine cycles, presented in Ref. [1].

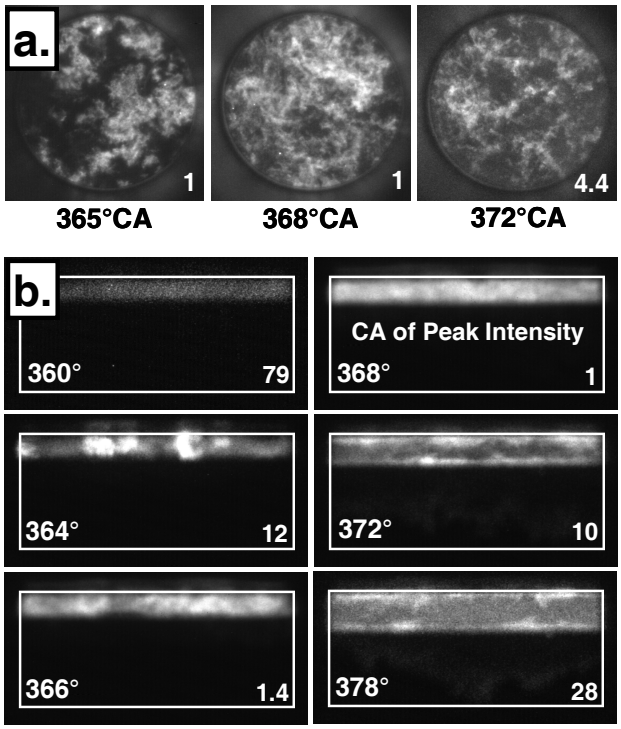

Figure 2. Chemiluminescence image sequences of HCCI combustion obtained through (a) the piston-crown, and (b) spacer-ring windows. Iso-octane, 1200 rpm, ϕ = 0.38, CA50 = 368° CA. Relative camera intensifier gains are given at the lower right of each image. Adapted from Ref. [1].

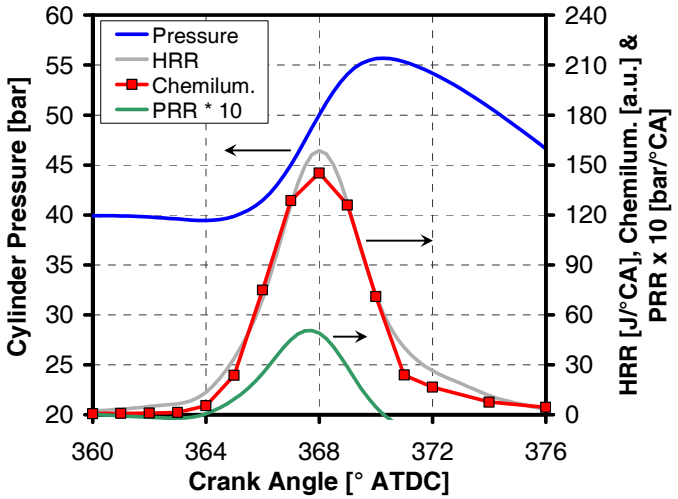

Figure 3. Cylinder pressure, HRR, PRR and average side-view chemiluminescence intensity corresponding to the images in Fig. 2. Adapted from Ref. [1].

Since the vast majority of combustion occurs in the central part of the charge up past the time of the maximum PRR (367.75° CA), it is mainly thermal stratification within the bulk gases that controls the maximum PRR and engine knock. Distinct boundary layer combustion does not begin until well after the time of maximum PRR. Therefore, thermal stratification between the bulk gas and the boundary layer has only an indirect effect on the knock limit, by reducing the portion of the charge in the bulk-gas.

The highly intermittent nature of the chemiluminescence in the central part of the charge indicates significant thermal stratification throughout this region. These thermal inhomogeneities presumably result from the transport of cooler gases from the near-wall region into the bulk gas by large-scale turbulence, but the mechanism is not well understood. Nevertheless, this bulk-gas stratification is critical to the high-load limit of HCCI, so a major portion of the current investigation focuses on planar temperature-map images and analysis showing the development of this bulk-gas thermal stratification.

EXPERIMENTAL SETUP

ENGINE FACILITY

The optically accessible HCCI engine shown schematically in Fig. 1 was used for the current study, as well as in Ref. [1]. The engine was derived from a Cummins B-series medium-duty diesel engine with a displacement of 0.98 liters/cylinder. As shown in the facility schematic in Fig. 4, the six-cylinder production engine was converted to single-cylinder operation by deactivating cylinders 1-5. The engine specifications and operating conditions are listed in Table 1. Detailed descriptions of the engine and facility may be found in Refs. [1 & 11], so only a brief description is given here.

TABLE 1. Engine Specifications and Operating Conditions

Displacement (single-cylinder)	0.981 liters
Bore	102 mm
Stroke	120 mm
Connecting Rod Length	192 mm
Geometric Compression Ratio (current study)	14:1
Geometric CR (chemilum. images, Ref. [1])	18:1
No. of Valves	4
IVO	0° CA*
IVC	202° CA*
EVO	482° CA*
EVC	8° CA*
Swirl Ratio	1.3
Fueling system	Fully Premixed
Engine Speed	1200 rpm
Intake Pressure	100 kPa (abs.)
Intake Temperature	170°C (443 K)
Coolant Temperature	100°C
Fuel	Iso-Octane with 2% Toluene

* 0° CA is taken to be TDC intake. The valve-event timings correspond to 0.1 mm lift.

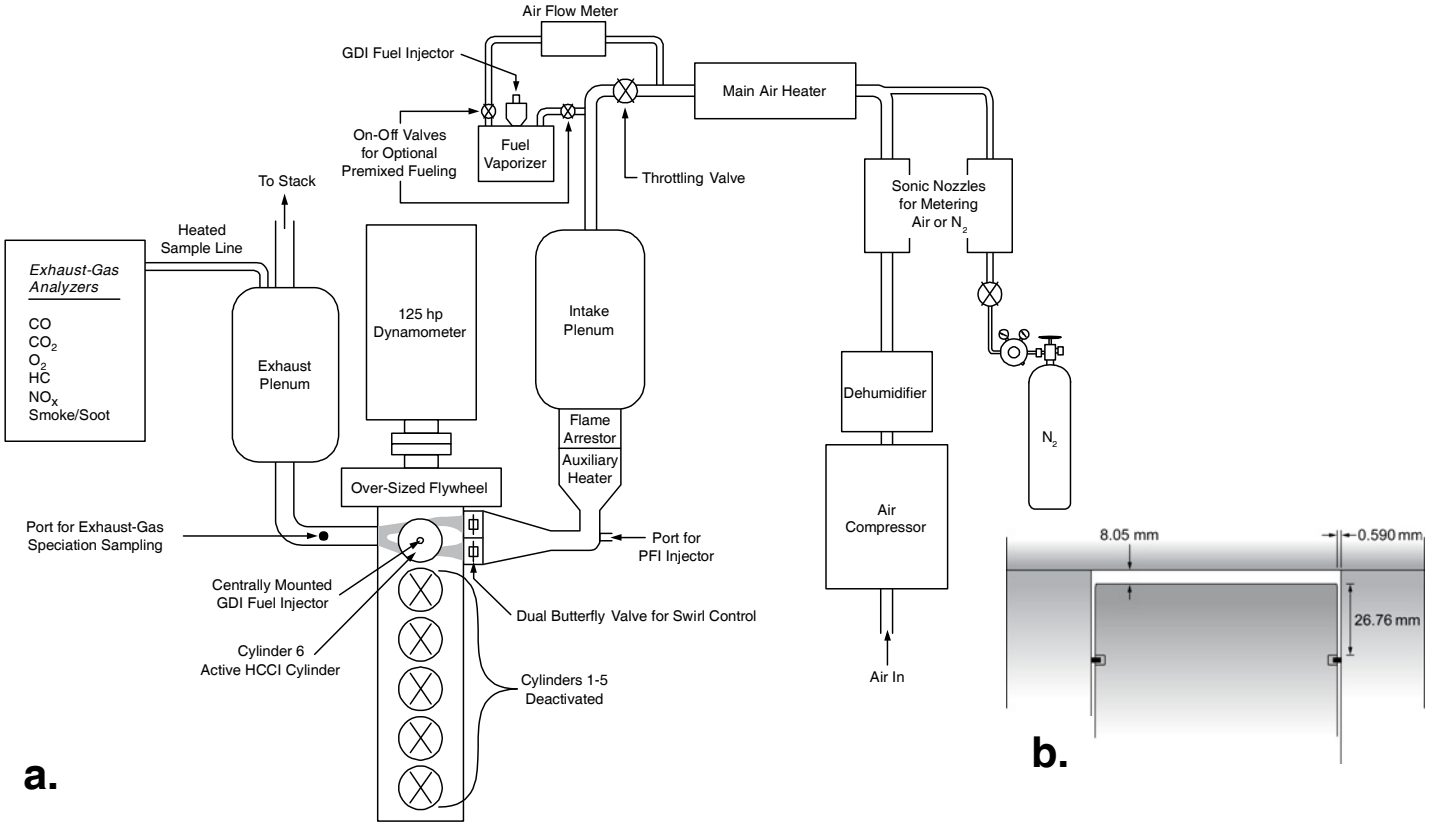

Figure 4. (a) Schematic of the HCCI engine facility. (b) Schematic of the CR = 14 optical-engine HCCI piston, at TDC.

As shown in Fig. 1, the engine utilizes a classic Bowditch piston arrangement with a large piston-crown window. The spacer ring that forms the top part of the cylinder wall contains three large windows to provide a horizontal view of the combustion chamber. This optical access extends downward 29.5 mm from the firedeck (*i.e.*, the flat cylinder-head surface). To allow horizontal optical access up to the firedeck surface, the spacer-ring and windows are recessed into the firedeck as shown in Fig. 1. The inner surfaces of the spacer-ring windows are curved to match the cylinder bore. As evident in Fig. 1, the flat piston-crown window and firedeck create a pancake combustion chamber. For the current study, the piston length was set to give a geometric compression ratio (CR) of 14; however, for the previous chemiluminescence imagine study presented above, a slightly longer piston was used to give CR = 18. Like most optical engines, the top ring-land crevice is quite tall to prevent the rings from riding over the edge of the spacer-ring windows. The volume of the top ring-land crevice is included in the geometric compression ratio. Figure 4b shows a detailed schematic of the pancake combustion chamber at top dead center (TDC), with dimensions.

The intake charge was fully premixed using the fueling system shown at the top of the schematic in Fig. 4a. This fueling system consists of an electrically heated fuel vaporizer and appropriate plumbing to ensure thorough premixing upstream of the intake plenum. A positive displacement fuel flow meter was used to determine the amount of fuel supplied. As discussed in the introduction, the intake charge was made inert by operating with nitrogen instead of air, to minimize quenching of the PLIF signal and to prevent breakdown of the toluene tracer. The nitrogen was metered and controlled by a sonic orifice with the upstream pressure being continually tuned by an electronically controlled pressure regulator. The nitrogen was electrically heated to the desired temperature. An auxiliary heater mounted close to the engine provided precise control of the intake temperature. For all data presented, the intake temperature was set to 170°C, which is representative of the intake temperatures required for iso-octane/air mixtures near the high-load limit with CR = 14 (ϕ = 0.4 – 0.5). However, intake temperatures ranging from 100° - 205°C were used to calibrate the temperature dependence of the PLIF signal. This resulted in peak compressed-gas temperatures of about 1000 K and 1080 K for the 170°C and 205°C intake temperatures, respectively. Since these temperatures are well below the 1150 K autoignition temperature of toluene, no thermal decomposition of the toluene tracer is expected.

All data were taken at an engine speed of 1200 rpm with the intake nitrogen flow adjusted to provide an intake pressure of 100 kPa, simulating naturally aspirated conditions. Prior to data acquisition, the engine was fully preheated to 100°C by means of electrical heaters on the "cooling" water and lubricating oil circulation systems. All data were taken under motored operation.

CONVENTIONAL DATA ACQUISITION

Cylinder pressure measurements were made with a transducer (AVL QC33C) mounted in the cylinder head approximately 42 mm off center. The pressure transducer signals were digitized and recorded at ¼° CA increments for one hundred consecutive cycles. The cylinder-pressure transducer was pegged to the intake pressure near bottom dead center (BDC) where the cylinder pressure reading was virtually constant for several degrees. Intake temperatures were monitored using thermocouples mounted in the two intake runners close to the cylinder head. In addition, a thermocouple mounted in the spacer ring with its junction embedded in the ring approximately 2 mm beneath the surface, 5 mm below the firedeck, provided an indication of in-cylinder surface temperatures by extrapolating its reading to the expected value at the surface. For all data presented, 0° crank angle (CA) is defined as TDC intake (so TDC compression is at 360°). This eliminates the need to use negative crank angles or combined BTDC, ATDC notation.

TEMPERATURE IMAGING DIAGNOSTIC

The diagnostic selected for the T-map imaging was single-line PLIF of toluene with excitation at 266 nm. The principle of this diagnostic is based on the temperature sensitivity of the PLIF signal of toluene in nitrogen. As first noted by Koban *et al.* [9], for homogeneous mixtures at constant pressure, the fluorescence from 266 nm excitation of toluene is a function of temperature only. The engine was supplied with a homogeneous fuel/nitrogen mixture, but pressure varies with crank angle, so it is necessary to account for pressure effects on the signal, as discussed below. Single-line temperature measurements are also possible with PLIF of ketone tracers [10,12] such as acetone or 3-pentanone. However, previous work in our laboratory [13] has shown that toluene provides a substantially better signal/noise (S/N) and requires lower tracer concentrations in the base fuel. In addition, the toluene-PLIF signal is much more sensitive to temperature variations [10]. With its strong signal, this toluene-PLIF diagnostic provides measurements with good precision, as discussed later.

For all measurements, the toluene was mixed to a concentration of 2% (by liquid volume) with the iso-octane fuel. Iso-octane was chosen as the fuel because it is a good surrogate for gasoline [14,15], and it does not fluoresce with UV excitation, unlike gasoline which has multiple fluorescing constituents. For all conditions studied, the same toluene concentration was supplied by fueling the engine at a rate that would correspond to an equivalence ratio (ϕ) of 0.4 if the nitrogen was replaced with air.

DIAGNOSTIC SETUP

The PLIF setup is shown in Fig. 5. The 4th harmonic of an Nd:YAG laser (266 nm) was used as the excitation source. A combination of spherical and cylindrical lenses formed the laser beam in to a thin sheet. Since

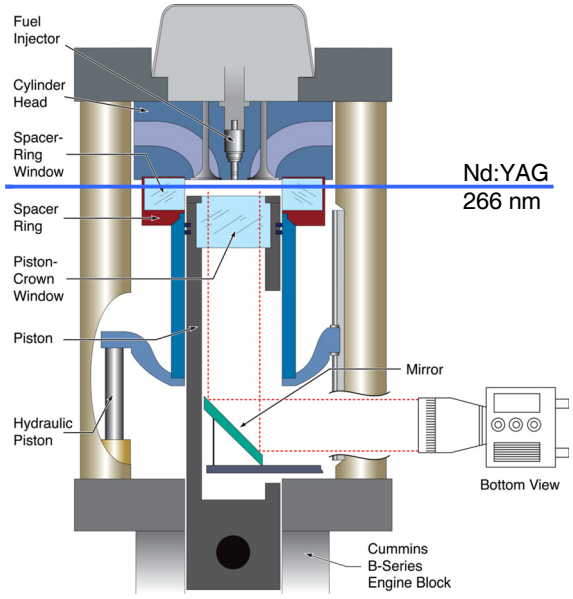

Figure 5. Engine schematic showing the setup for PLIF imaging.

the 4th harmonic laser-beam had a very irregular profile, the laser sheet was overly expanded, so an iris could be used to isolate the most intense and uniform portion of the sheet. In this manner, the laser-sheet intensity in the engine varied less than 20% from the center to the edge. The final sheet width occupied the full width of the spacer-ring window. These windows were designed to have the same inner and outer radii of curvature to prevent the window from acting as a lens. However, the windows were thick, so the focusing effect could not be completely eliminated, and the sheet width slightly converged, from 43 to 39 mm over the field of view in the cylinder. The sheet exited the engine through the spacer-ring window on the opposite side and was captured by a beam dump. Except for the outer boundary-layer measurements, discussed later, the laser sheet was angled slightly downward to prevent damage from back reflections. The laser-sheet energy measured after the iris was 24 mJ/pulse. The final laser-sheet formation optics were mounted on a motorized translating stage that allowed the sheet to be positioned at any desired elevation below the firedeck. For most data, the sheet was positioned in the mid-plane of the pancake combustion chamber (most representative of the bulk gas), which varied from 4 to 16 mm below the firedeck for 360 to 305°CA, respectively.

An intensified CCD camera, sensitive in both the visible and UV ranges, captured the PLIF images through the piston-crown window at a resolution of 640 x 480 pixels. The camera-intensifier gate and laser pulse were synchronized with the engine to obtain images at any desired crank angle. Toluene fluoresces in the UV (265 – 330 nm), and was imaged with a 45 mm f/1.8 fused silica camera lens using a 277 nm long-wave-pass (LWP) and a UG5 UV-bandpass (mainly between 220 and 400 nm) filter. The 277 nm LWP filter blocked elastic scattering from the excitation laser. The UG5 filter substantially reduced undesired interference from visible and near-IR light emission, thought to be largely due to fluorescence of residual oil in the metal (cylinder head and valves) that was excited by scattered and reflected laser light. The piston-crown window provides a field of view of 70 mm in diameter, which corresponds to approximately half of the area of the 102 mm diameter combustion chamber. For all T-map images presented, a white circle around the imaged area shows the limits of the 70 mm field of view.

Initially, the laser sheet was configured using a 770 mm lens to form a waist near the center of the combustion chamber that was approximately 0.2 mm thick. For images acquired near TDC (pressure ~ 29 bar), this provided images of nearly uniform intensity across the field of view. However, at early crank angles the images had a dark area at the laser-waist location as shown in the left-hand image of Fig. 6. (Note that for all images presented the laser sheet propagates from right to left.) This effect is thought to result from photo-bleaching of the ground state. It is very pronounced at 305°CA because at the lower pressures (~4.5 bar) the collisional rates are not adequate to repopulate the ground state at the rate it is being depleted by laser-pumping to the excited state. Although laser-sheet normalization (discussed below) can largely remove this effect, S/N would be poor in this waist region. Therefore, the optics were reconfigured with a 1550 mm lens forming the waist. Additionally, the waist was positioned beyond the cylinder so the sheet thickness varied from 1.6 to 0.7 mm across the field of view. This increased thickness was more than that required to eliminate photo-bleaching, but the waist could not be moved closer to the cylinder without causing window damage. Fortunately, this thicker sheet still provides sufficient resolution to visualize the thermal stratification. With this long focal-length spherical lens forming the waist, a combination of two diverging lenses (-750 mm and -30 mm) was used to expand the beam into a sheet. This laser-sheet configuration resulted in a uniform image intensity at 305°CA as shown by the right-hand image in Fig. 6.[2]

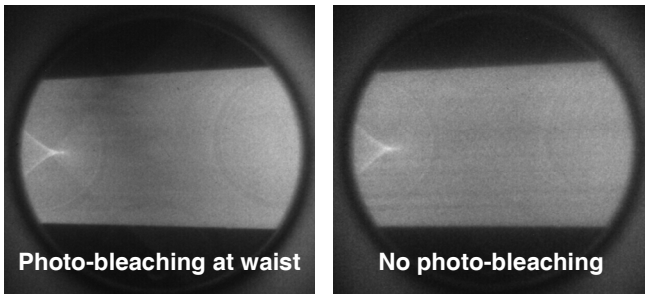

Lens f.l. = 770 mm
Waist near center
Thickness = 0.8 - 0.2 mm

Lens f.l. = 1550 mm
Waist beyond cylinder
Thickness = 1.6 - 0.7 mm

Figure 6. Toluene PLIF images at 305°CA, with different sheet-forming optics.

[2] The bright triangular-shaped region at the left side of both images in Fig. 6 is a focused back reflection from the exit window. This non-uniformity in laser intensity was removed by the flat-field normalization process discussed in the next subsection.

IMAGE CORRECTION & CALIBRATION

Corrections – Using this new laser sheet configuration, images were acquired in sets of 40 (from separate cycles) at each measurement condition. Several basic corrections were applied to these raw PLIF images before converting them to temperature maps using the calibration discussed below. Since camera intensifier gain was adjusted for each condition, the images were normalized against a reference gain using a calibration curve. The laser energy varied slightly from shot to shot, so the energy of each pulse was measured and normalized against a reference value. Even with the fuel turned off, faint outlines of the valve pockets could be viewed in the images, which is thought to result from fluorescence of residual oil in the metal that was excited by scattered laser light. To correct for this, background images were acquired with the fuel turned off, and the average background image of a set of 40 images was subtracted from each PLIF image. Since toluene number density varies with crank angle and intake temperature, the images were normalized to a reference density using the known amount of fuel supplied and the change in cylinder volume. Camera and laser-sheet non-uniformities that were consistent from shot to shot were removed by normalizing the individual images by a flat-field image obtained by averaging the 40 images from the data set. (Shot-to-shot variations in the laser profile are discussed in the next subsection.) Note that this normalization will remove any temperature non-uniformities that are consistent from cycle to cycle; however, examination of these averaged images showed that they were very uniform (*i.e.*, there is no detectable repeating pattern to the temperature fluctuations), so the normalization should not affect the measured thermal stratification.

Laser-sheet attenuation across the image was small, and the flat-field normalization procedure described above will remove its effect from the images. However, the normalization cannot be used for the calibration procedure, described in the next paragraph. Therefore, an attenuation correction was applied by measuring the change in intensity across the field of view of the average image (of the 40-image set) at each condition and applying Beer's law to determine an absorption coefficient. Using this coefficient, the attenuation from the entrance window to each pixel location was computed, and a correction was applied. A list of all corrections applied is given in Table 2.

Temperature and Pressure Calibrations – To calibrate the temperature sensitivity of the toluene-PLIF signal, images were acquired for four different intake temperatures: 100, 135, 170, and 205°C. Also, for each intake temperature, calibration images were acquired at each crank angle of interest since changes in pressure with crank angle can also affect the PLIF intensity. The laser-sheet elevation was adjusted with crank angle so all calibration images were acquired in the midplane of the pancake combustion chamber. After acquiring these images, all the basic corrections discussed in the previous paragraph were applied, except the flatfield normalization. For calibration analysis, an interrogation region (approximately 25 by 25 mm) was selected near the center of the imaged area. The spatially averaged intensity of this region, also averaged over the forty images acquired for each condition, was then correlated with the expected in-cylinder temperature for each condition computed using the following two-step process: 1) in-cylinder BDC temperatures were calculated using the method developed earlier in our laboratory [16], and 2) the change in temperature from this BDC temperature was computed assuming adiabatic compression following the measured pressure trace (ensemble-averaged over 100 cycles) and using real-gas properties that were adjusted at each time step. In this manner, the computed temperature accounts for the overall effects of heat transfer (through the measured pressure trace), but assumes the central interrogation region itself is adiabatic, *i.e.* it assumes that the interrogation region is part of an adiabatic core.

TABLE 2. Image Corrections and Uncertainties

Corrections:
Camera gain
Normalization by total laser energy
Background subtraction
Number density
Laser-sheet attenuation
Pressure
Flat-field correction (normalization by average image)
Absolute-Accuracy Uncertainties:
Calibration interrogation-regions were not adiabatic
Variations in shot-to-shot laser-sheet energy not captured by total beam-energy normalization
Precision Uncertainties:
Shot noise
Shot-to-shot variations in the laser-sheet profile

This calibration approach yields a separate image-intensity vs. temperature calibration curve for each crank angle. These curves can then be used directly to calibrate the individual images at each crank angle. However, a small error would result because the pressure at any given crank angle is not exactly the same for all four intake temperatures due to differences in heat transfer. It is also of fundamental interest to investigate the effects of pressure on the PLIF signal. Accordingly, a separate calibration was conducted in which the intake pressure was varied from 60 to 205 kPa (abs.) with a fixed intake temperature of 100°C. Applying this pressure calibration to the temperature-calibration data, which was acquired for the baseline intake pressure of 100 kPa, allows the individual temperature calibrations for each crank angle (which are each at a different pressure) to be presented on a single combined plot, as shown in Fig. 7. As can be seen, the individual calibration curves align fairly well after applying the pressure correction, and it might be possible to fit a single temperature calibration curve for the entire range. However, separate linear-fit calibration curves for each crank angle were used, as shown in the figure. In this manner, the calibration curves fall more closely to the calibration data points at each crank angle,

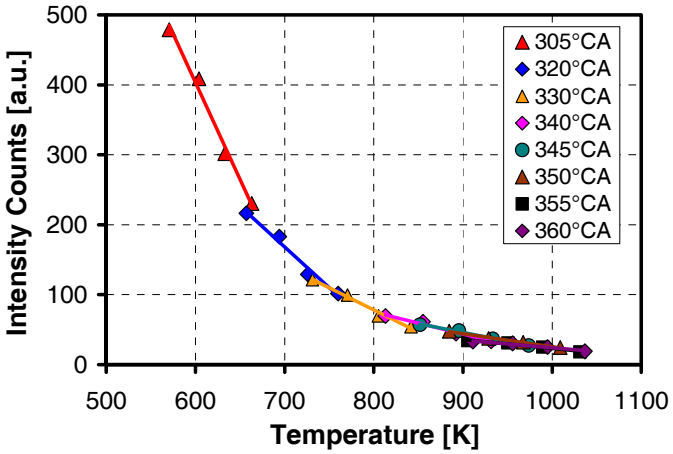

Figure 7. Calibration curves for converting PLIF intensity to temperature. The data have been adjusted for pressure changes between crank angles.

which should be more accurate. Another advantage to this approach is that uncertainties in the pressure calibration have almost no effect (since pressures are similar for the four data points at each crank angle). This was considered important since some extrapolation of the pressure-calibration data was required.

It may be noted that Fig. 7 shows no calibration curves for crank angles after TDC. This is because analysis showed that the temperatures of the interrogation region for crank angles after TDC were significantly colder than those for the corresponding crank angles the same number of degrees before TDC. This indicates that significant heat transfer has occurred in the interrogation region for the after-TDC images. Thus, there would be a significant discrepancy in applying the calibration temperatures, which are based on the assumption of an adiabatic-core region. Since the before-TDC images are less affected by heat-transfer and the pressures are similar to those the same number of CA degrees after TDC, it was deemed more appropriate to use the calibration curves for the corresponding crank angles before TDC for analyzing the after-TDC images. As discussed in the next subsection, some heat transfer occurs even for the later crank angles before TDC, but conditions are still closer to adiabatic than they are after TDC.

To obtain T-map images, the calibration curves in Fig. 7 were applied to the PLIF images after first making all the basic corrections listed above. Also, a pressure correction was applied to the images so they were compatible with the pressure-corrected calibration curves (Fig. 7). Finally, a 3 by 3 median filter was applied to the T-map images to reduce noise. This should have virtually no effect on the image resolution since 3 pixels corresponds to approximately 0.5 mm, which is less than half of the average laser-sheet thickness. Figure 8 presents an example of the conversion of raw PLIF images at 360°CA (TDC) to T-map images. Note that the high-intensity regions in the raw images correspond to colder regions as indicated by the calibration curve in Fig. 7.

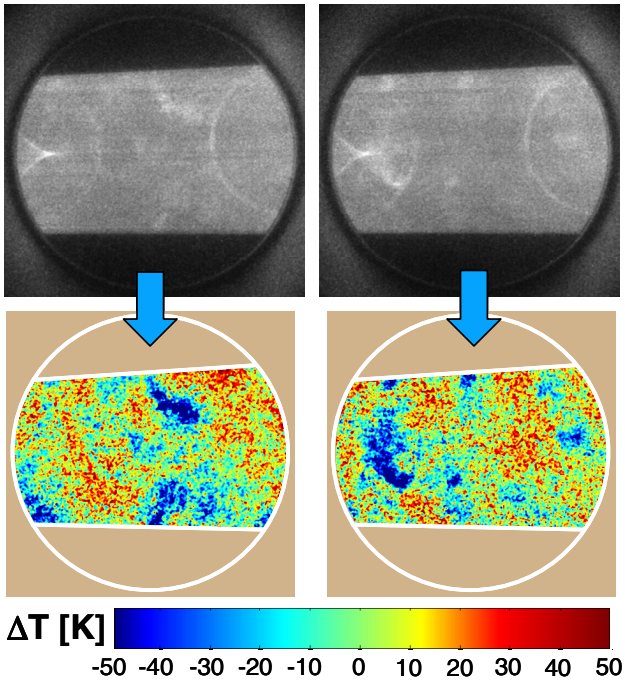

Figure 8. Conversions of raw PLIF images to T-maps for two separate cycles at 360°CA, 4 mm below the firedeck (mid-plane of chamber).

ACCURACY and PRECISION

Absolute Accuracy – The absolute accuracy of these single-line T-map images is determined mainly by the accuracy of the calibration technique. This relies on an assumption that the interrogation region used for calibration is adiabatic, even though the rest of the charge may experience heat transfer. However, as indicated by the example images in Fig. 8, the central region is not necessarily adiabatic for crank angles near TDC. In fact, a detailed analysis shows that the location of the bulk-gas thermal stratification is sufficiently random that the thermal fluctuations in the central interrogation region are about the same as those of the entire image. The accuracy could be improved by setting the intensity of the hottest regions, which are distributed throughout the charge, to the computed adiabatic (following the measured pressure trace) temperature. An analysis shows that this would have the effect of shifting the calibration curves in Fig. 7 downward, but it would have little effect on the slope of the linear fits. Therefore, it would reduce the absolute temperatures by as much as 25 K at TDC, but would have almost no effect on the spread of temperatures measured at any given crank angle.

Another error in the absolute accuracy could result if variations in the shot-to-shot laser energy reading do not match the changes in the laser sheet intensity in the engine. This is possible because only a portion of the total laser sheet was used in the engine, whereas the energy reading included the entire beam cross section. The magnitude of this error was examined by acquiring images while the engine was stationary, with nitrogen and toluene-doped fuel flowing slowly through the engine. Under these conditions the in-cylinder temperature should be steady from shot to shot, so variations in the

image intensity are due only to variations in the laser sheet energy. Averaging the PLIF intensity over a large portion of the laser sheet and normalizing by the laser energy reading showed that the normalization reduced the shot-to-shot variations in intensity, but a standard deviation (std-dev) of 2.2% remained. Converting this to an equivalent temperature uncertainty yields a std-dev of 2.4 K (0.38%) at 305° CA and 5.0 K (0.50%) at 360° CA. In future studies, this uncertainty could be removed by directly measuring only the energy in the portion of the laser sheet used in the engine.

However, the main purpose of the current study is to determine the amount and distribution of the thermal stratification at each crank angle, so high accuracy in the absolute temperature is not required. Therefore, the above-mentioned correction to the calibration was not applied (*i.e.* the absolute temperatures are based on setting the average intensity of the interrogation region to the adiabatic temperature), and no effort was made to directly measure only the energy within the laser sheet. Furthermore, most results are presented in terms of a $\Delta T = T - T_{average}$ at each crank angle, making these uncertainties in the absolute temperature irrelevant.

Precision – Although absolute accuracy is not a major concern for this study, the precision of the measurements at each crank angle is important. Therefore, an analysis was conducted to estimate the effect and magnitude of the various noise sources affecting the precision of the relative temperatures within a given image.

Shot noise, which results from the limited number of photons collected, is the largest source of noise in these single-shot images. Because it is related to the PLIF intensity, the shot noise is greatest near TDC when the charge is hottest, and therefore has the lowest intensity (see Fig. 7). To determine the magnitude of the shot-noise, images were acquired of a piece of plain white paper placed in the image plane with the engine stopped, the laser turned off, and the paper illuminated by an incandescent bulb. The amount of light collected (*i.e.* the image brightness) was adjusted to match values typical of the toluene PLIF images at the various crank angles. Sets of 100 images were acquired for each brightness setting. For each set, the average intensity of each image was normalized to match the average intensity of the entire set to remove any image-to-image variations in average intensity. Although the average image intensity was constant, the intensity reading of any given pixel varied slightly from image to image due to shot noise. The images were then converted to temperature space using the calibrations in Fig. 7, and the standard deviation (std-dev) was computed of the "temperature" of each pixel over the 100-image set. Finally, these individual-pixel std-dev values were averaged over an interrogation region corresponding approximately to the active area of the PLIF images. For TDC, this gives a std-dev = 8.4 K, or 0.85% of the 990 K temperature, and for the coldest condition studied, 305° CA, the std-dev = 3.1 K, or 0.49% of the 640 K temperature.

Another potential noise source arises from shot-to-shot variation in the laser sheet profile. As discussed previously, the flat-field normalization removes the effect of laser-sheet variations that are consistent from shot to shot. However, if the laser profile of an individual shot varies from the mean, it will artificially increase the measured temperature variation for the 40-image dataset. To investigate this, an intensity profile across the laser sheet was computed for each individual image by ensemble averaging the intensities of 145 columns of pixels (*i.e.* the average profile for a region approximately 23 mm wide). This wide band should minimize the effect of real temperature fluctuations across the image, but it will not necessarily eliminate them. Therefore, only images from the mid-plane at 305°CA, which have almost no temperature fluctuations (as shown later), were used to estimate the magnitude of this noise source. (Since there is still a possibility of temperature fluctuations contributing slightly to the apparent laser-sheet profile variations, these noise estimates should be considered an upper bound.) The individual image profiles were compared to the mean profiles of their respective datasets (averaged over the same columns) after the profiles had been converted to temperature space using the calibrations in Fig. 7. This analysis indicated that shot-to-shot variations in the laser profile produce an uncertainty in the temperatures ranging from a std-dev = 2.4 K or 0.24% of the 990 K temperature for TDC to 1.2 K or 0.19% for the 640 K temperature at 305° CA.

Assuming that the shot noise and the noise due to variations in laser sheet profile are independent, these errors can be combined as the square root of the sum of the squares (*i.e.* in quadrature) to get an overall uncertainty (one standard deviation) of 8.8 K at TDC and 3.3 K at 305° CA. The relationship of these uncertainties to the apparent spread in temperatures derived from the images will be discussed with the presentation of the temperature PDFs in the next section. Table 2 provides a list of the uncertainties affecting the accuracy and precision of the temperature data.

RESULTS AND DISCUSSION

EVOLUTION OF THERMAL STRATIFICATION

Figure 9 shows the evolution of the in-cylinder bulk-gas temperature for the 170°C intake temperature used for data acquisition. These temperatures were derived from the BDC temperature and the pressure trace as described in the Diagnostic section. As can be seen, the BDC temperature (180° CA) is only 24 K above the wall temperature,[3] which is estimated to be about 400 K based on the surface temperature derived from the spacer-ring thermocouple. Since the results in Ref. [1] suggest that natural thermal stratification arises mainly from wall heat transfer and turbulent convection [1], stratification is not expected to be significant until the gas temperature has risen well above the wall temperature.

[3] The BDC temperature is about 20 K lower than the measured intake temperature as a result of heat transfer during the intake process [16].

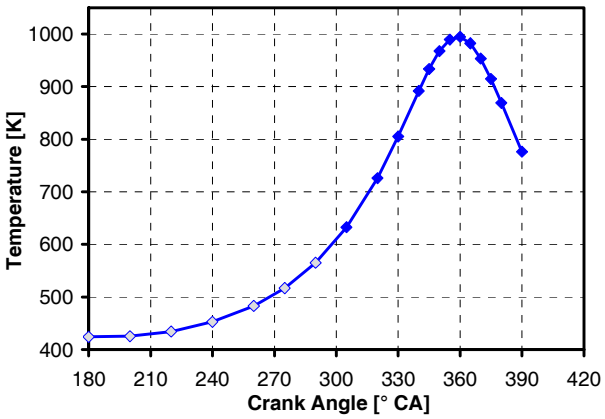

Figure 9. In-cylinder bulk-gas temperature for the 170°C intake temperature, computed with the technique used for calibration. Blue filled symbols indicate crank angles at which images were acquired.

Furthermore, thermal stratification of the bulk gas requires time for convection to bring the cooler near-wall gases into the central part of the charge. During the first part of the compression stroke, Fig. 9 shows that the in-cylinder temperature rises only slowly. Even at 305° CA, the start of the PLIF image acquisition, the temperature has only increased to 632 K. Therefore, significant bulk-gas stratification would not be expected until later crank angles. This reasoning is supported by KIVA calculations previously conducted on a matching all-metal version of the optical engine used in the current study (albeit at a higher CR = 18) [17], which are reproduced in Fig. 10. As shown, the thermal width of the 85% hottest mass doesn't begin to increase substantially until 300 - 310° CA. Therefore, natural thermal stratification is expected to develop progressively during the latter part of the compression stroke.

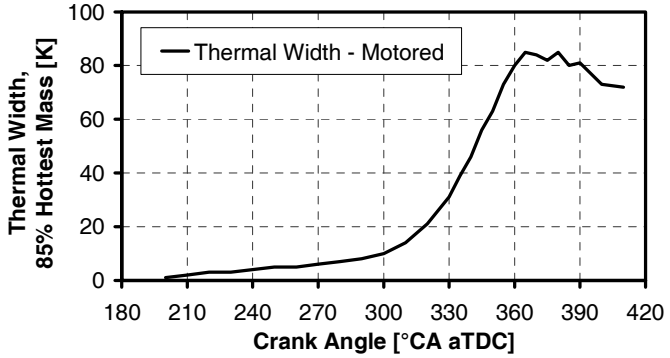

Figure 10. KIVA results showing the evolution of the thermal width for a matching all-metal version of this engine with a CR = 18 piston. Adapted from [17].

Figure 11 presents a temporal sequence of T-map images from 305° - 390° CA at the mid plane of the combustion chamber. (The laser sheet elevation was adjusted with crank angle from 20 mm below the firedeck at

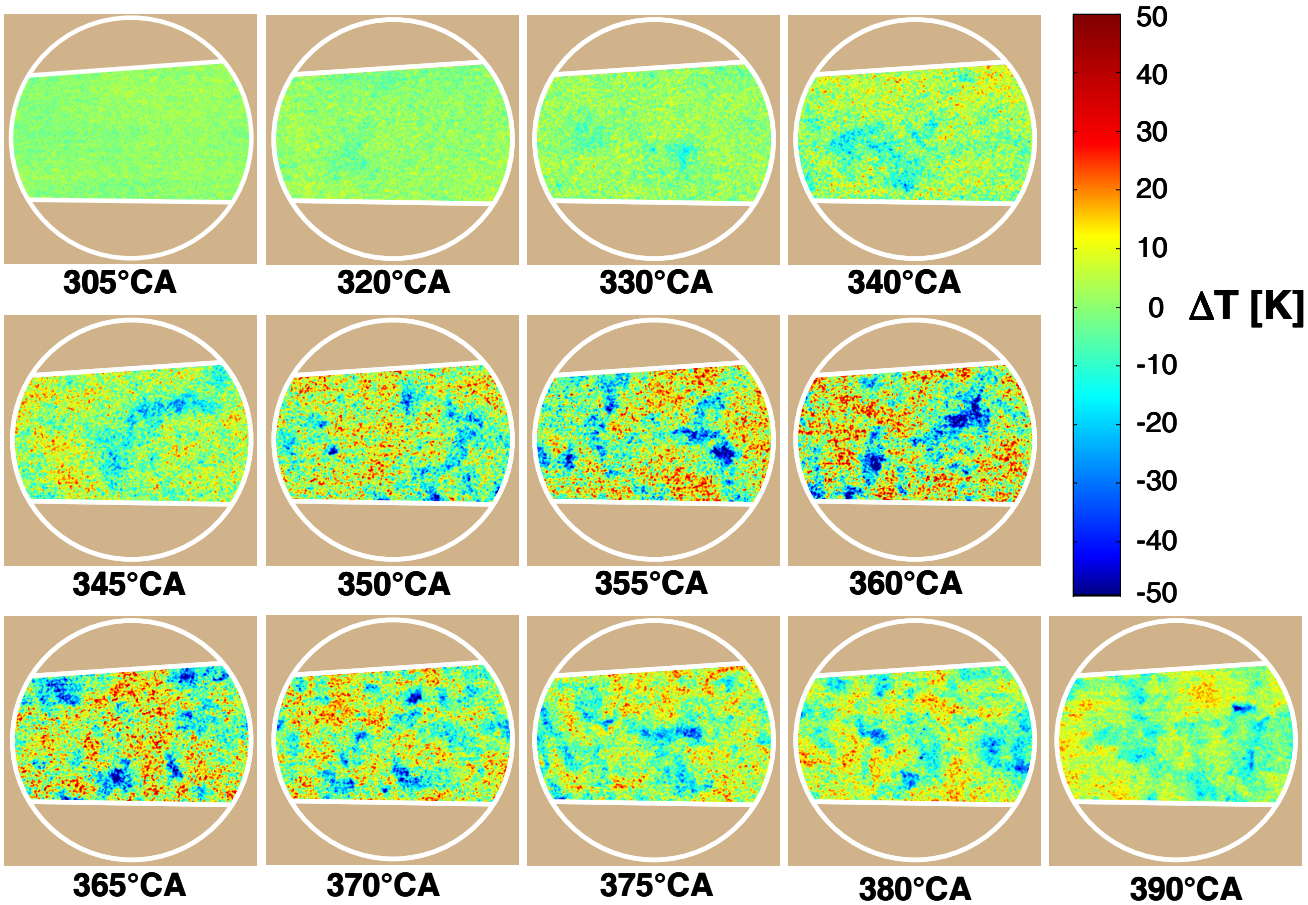

Figure 11. Temporal sequence of T-map images at the mid plane of the pancake combustion chamber. The white lines outline the limits of the laser sheet and the 70 mm diameter field of view through the piston-crown window.

305° CA to 4 mm below it at 360° CA.) These images have been selected as being representative of the sets of forty images acquired at each crank angle from forty separate cycles. The false-color temperature scale shows the change in temperature relative to the mean of each image (ΔT), making the variations in temperature more clearly evident. As expected, there is no noticeable stratification at 305° CA, and even as late as 330° CA, the temperature varies only slightly over the field of view. By 340° CA, some distinct thermal stratification is present, and the amount increases through 360° CA (TDC). This increase in thermal stratification occurs both in terms of the number of hot and cold regions and in terms of the temperature difference between these regions. Beyond TDC the number of hot and cold pockets continues to increase, but the amplitude of the hot-to-cold variations appears to decrease again.

In addition to these larger-scale temperature variations, the images in Fig. 11 show a fine-grained speckle pattern. This is barely noticeable at 305° CA, but moving along the sequence to 360° CA, it becomes progressively more noticeable. It is particularly evident in the hotter (red) regions of the 355° and 360° CA images, which are at the highest temperature. This graininess is the result of shot noise, which increases as the signal intensity decreases with increasing temperature, as discussed in the previous section. This noise will contribute to the apparent variation of temperature within the images when they are analyzed using probability density functions, and it must be accounted for when computing the magnitude of the thermal stratification, as will be discussed in the next subsection.

It is also of interest to investigate the spatial scale of the bulk-gas thermal stratification. This stratification arises from colder near-wall gases being transported into the hotter gases in the central part of the chamber. As a result, the structure of the colder regions should be most representative of the scale of the flow structures responsible for the convective transport. These structures are somewhat random in shape and a detailed auto-correlation analysis would be required to rigorously define a spatial scale, which is beyond the scope of the current study. However, an indication of this scale can be quickly obtained by measuring typical diameters or widths of the cold pockets in the images. This gives a size on the order of 5 – 11 mm for these structures in the 345 – 365° CA images. (Note that for longer regions such as the one in the upper-right quadrant of the 345° CA image, only the width of the region was considered for this measurement.) This spatial dimension is comparable to the 8 mm piston-to-firedeck clearance height at TDC. It is interesting to note that a similar correlation may be found between the width of the first bright-chemiluminescence regions in Fig. 2b at 364° CA and the 6 mm clearance height at 364° CA for the CR = 18 configuration used to acquire these images [1]. Although the first chemiluminescence marks the hottest regions, these similar findings from two separate data sets strongly suggests a relationship between the scale of the flow structures creating the thermal stratification and the clearance height.

PDF ANALYSIS

Probability density functions (PDF) provide a method for quantitative analysis of the thermal stratification and other features of the T-map images. Detailed analysis is presented for 305° and 360° CA, which are the coldest and hottest conditions imaged, and as such, they bracket the behavior at the other crank angles.

Absolute Temperature Variations – Figure 12a presents mass-weighted PDFs of all forty images acquired at 305° CA. As can be seen, the PDFs show a spread in the mean temperatures as well as in the variation of temperature within each image. The std-dev of the mean temperatures from the PDFs is 2.6 K, and the difference between the hottest and coldest cycles (the maximum spread) is about 11 K. The subsection on Absolute Accuracy shows that the large majority of this cycle-to-cycle variation can be attributed to laser-sheet intensity variation, since iso-thermal conditions showed a std-dev of 2.4 K. It is unclear if the small difference between these standard-deviation values is statistically significant; nevertheless, it is interesting to compute the real cycle-to-cycle temperature fluctuations expected from these measurements. Since the laser-intensity variations are not correlated with the real temperature fluctuations, these two sources of measurement variation should contribute to the total variation as the square root of the sum of the squares. Solving this relationship for the portion of the measured cycle-to-cycle variation due to real fluctuations (*i.e.*, $\sqrt{2.6^2 - 2.4^2}$) gives a std-dev of 1.1 K, which corresponds to a maximum spread of 4.6 K assuming that the ratio between std-dev and maximum spread remains the same as that of the direct measurement. Thus, the data indicate a small mean bulk-gas temperature variation even at 305° CA. Since the difference between the bulk-gas and wall temperatures is still small at 305° CA, and there has been little time for heat transfer to cause this fluctuation, it most likely arises from small cycle-to-cycle variations in the BDC temperature resulting from variations in heat transfer during the intake. Based on the effect of compression, a std-dev = 0.7 K at BDC would be required to produce this std-dev = 1.1 K at 305° CA.

Examination of the PDFs in Fig. 12b for 360° CA shows that by TDC, cycle-to-cycle variations of the mean temperature of the PDFs have increased (note the change of scales between Figs. 12a and 12b). The std-dev and maximum spread of the 40 cycles are 5.7 K and 23.5 K, respectively. This compares with an expected std-dev from laser-sheet intensity variations of 5.0 K. Thus, a large portion of the increased cycle-to-cycle variations in measured temperature are due to the increased sensitivity of the temperature measurement to laser-sheet intensity variations. Following the procedure described in the previous paragraph, the portion of the measured cycle-to-cycle variations attributed to real temperature fluctuations is a std-dev = 2.9 K, with an equivalent maximum spread = 11.8 K.

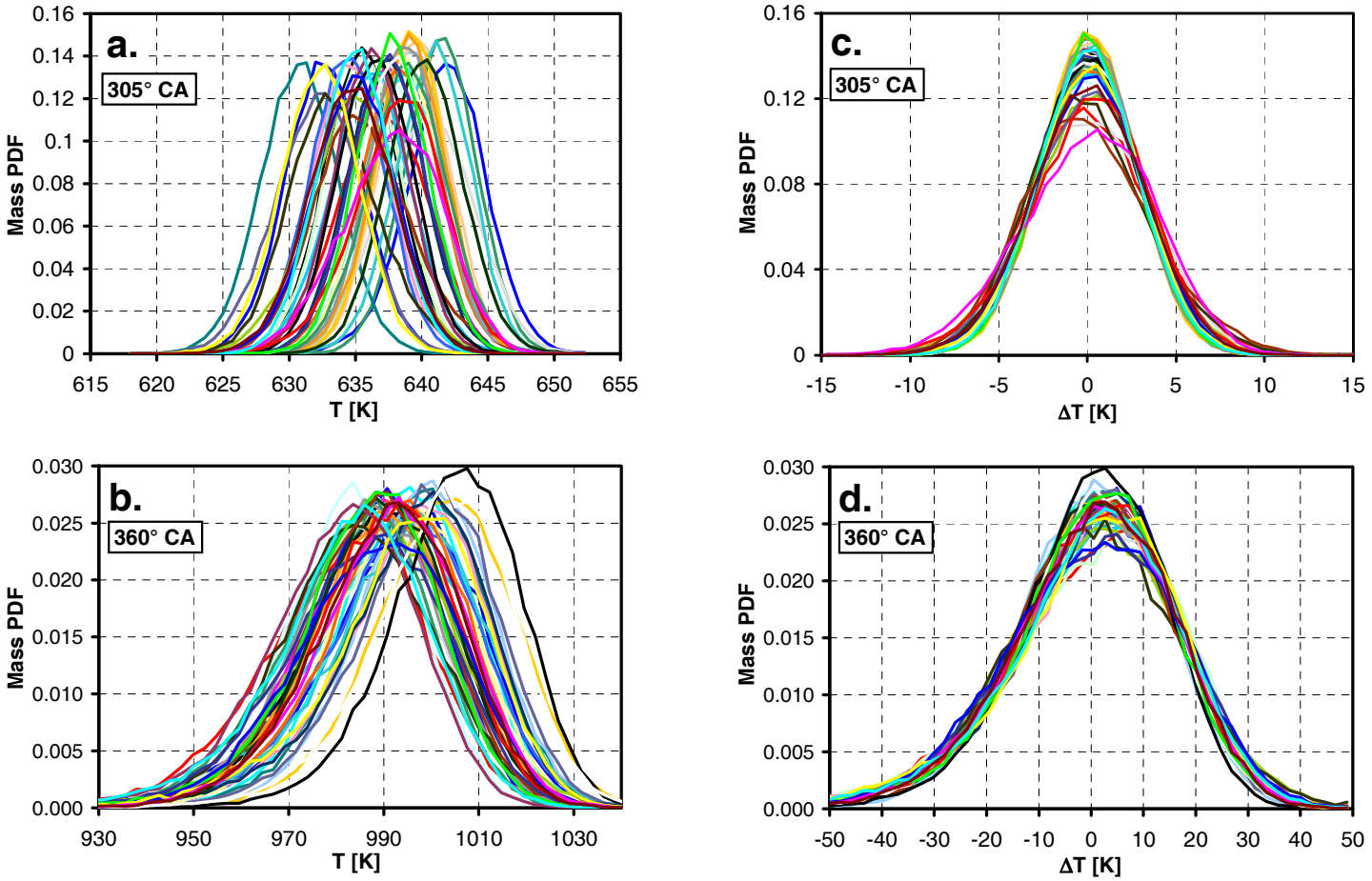

Figure 12. Mass-weighted PDFs derived from the T-map images for all 40 cycles acquired at 305° and 360° CA. 12a and 12b display the PDFs in real temperature, showing cycle-to-cycle variation of the mean temperature. 12c and 12d display the same PDFs in terms of ΔT with respect to the mean temperature, *i.e.* with the mean temperatures aligned.

Analysis indicates that these real cycle-to-cycle mean temperature variations at TDC result from a combination of the existing variations at 305° CA and heat transfer as the charge is compressed to TDC. Compression will increase the variations already present at 305° (std-dev = 1.1 K) to a std-dev = 1.7 K at 360° CA, with the remainder of the temperature variations at TDC resulting from variations in heat transfer from cycle-to-cycle during the latter part of the compression stroke. Assuming that the variations from these two sources are uncorrelated, cycle-to-cycle variations in heat transfer are responsible for variation in the mean TDC temperature of about 2.3 K and 9.4 K for the std-dev and maximum spread, respectively.

Since the shapes of the PDFs are nearly the same for each cycle (as discussed below), the cycle-to-cycle temperature variations of the hottest regions, which control autoignition, will be about the same as those of the mean temperature. The magnitude of this variation (std-dev = 2.9 K and maximum spread = 11.8 K) compares well with data on cycle-to-cycle variations for fired operation with iso-octane in the matching all-metal version of the optical engine used in the current study. The metal-engine operating conditions (speed and intake temperature) were very similar to those used in the current motored-engine study [18]. These fired data showed a standard deviation of CA50 of 0.75° CA with a maximum spread of 4.25° CA, for a 100-cycle dataset.[4] For the metal engine, the sensitivity of CA50 to changes in intake temperature was also studied (Fig. 22b in Ref. [18]). These intake temperature variations were then converted to estimated compressed-gas temperatures following a procedure similar to that used for the calibrations of the current study. Based on this analysis, the measured cycle-to-cycle variation in CA50 corresponds to variations in the TDC temperature of std-dev = 2.3 K and maximum spread = 11.6 K. These values closely match those from the PLIF data (std-dev = 2.9 K, maximum spread = 11.8 K), providing an independent check on the validity of the cycle-to-cycle temperature variations determined with the PLIF technique.

Relative Temperature Variations – Aligning the mean temperatures of the mass-weighted PDFs in Figs. 12a and 12b allows investigation of the cycle-to cycle variations in the shape of the PDF. Figures 12c and 12d present the aligned PDFs for 305° and 360° CA, respectively. As can be seen, for both crank angles, the distri-

[4] The average CA50 = 368.5° CA, and the supplied equivalence ratio was 0.4.

bution of temperatures is nearly the same for every cycle. Analysis of the ensemble-average of the PDFs in Figs. 12c and 12d shows that the width between the 5 - 95% distribution points of the PDFs, the thermal width (TW), varies from 10 K at 305° to 52 K at 360° CA. Assuming a normal distribution (*i.e.* 5 to 95% = -1.645*std-dev to +1.645*std-dev), this corresponds to standard deviations of 3.0 K for 305° and 15.9 K for 360° CA.

As discussed previously under the "Precision" subsection, the main sources of uncertainty in the distribution of temperatures within an image are shot noise (most significant) and shot-to-shot variations in the laser-sheet profile (less significant). For 305° CA, the combined uncertainty from these two sources yields a std-dev = 3.3 K. This value slightly exceeds the 3.0 K std-dev derived from the PDFs in Fig. 12c. The cause of this discrepancy is unclear. Perhaps it is a result of the small sample size or the assumption of a normal distribution not being completely valid. Since the uncertainty from shot noise and laser-sheet profile variations accounts for all the measured temperature distribution in the images at 305°, these data indicate that the temperature of the bulk gases is essentially uniform at this crank angle, in agreement with the appearance of the image in Fig. 11.

However, by 360° CA (TDC) significant thermal stratification of the bulk gas has developed. The image PDFs show a std-dev = 15.9 K (5-95% TW = 52 K), whereas the combined shot-noise and laser-profile std-dev = 8.8 K. Assuming that the contribution of this combined noise source is not correlated with the real temperature variations, it can be subtracted in quadrature from the measured temperature variation (*i.e.*, $\sqrt{15.9^2 - 8.8^2}$). This yields a real temperature variation across the images of std-dev = 13.3 K and 5 – 95% TW = 44 K assuming a normal distribution.[5]

PDF and Thermal Width Variation with Crank Angle – Similar to the PDFs in Figs. 12c and 12d, the individual-cycle PDFs for the other crank angles examined have similar shapes when their mean temperatures are aligned. Ensemble-averaging these aligned PDFs provides a means for comparing trends with crank angle, as shown in Fig. 13. As can be seen, the PDF at 305°CA is very narrow, and the analysis presented above indicates that this apparent TW is essentially just the "noise" in the measurement. From 305° to 330° CA, the TW increases slightly, but from 330° to 340° CA a significant broadening of the PDF occurs. This is in agreement with the images in Fig. 11, which show only slight non-uniformities through 330° CA, but a more definite cooler region at 340° CA, indicating that the convection of colder near-wall fluid has begun to reach the mid-plane of the combustion chamber. Significant broadening of the PDFs

[5] The assumption of a normal distribution is not completely valid for 360° CA since the PDF has a slight asymmetry, as discussed below. However, the same real TW = 44 K can be obtained by assuming only that the combined shot-noise and laser-profile variation is normally distributed to obtain a noise 5 – 95% TW = 28.9 K, which can be subtracted in quadrature from the measured TW = 52.3 K to obtain a real TW = 44 K.

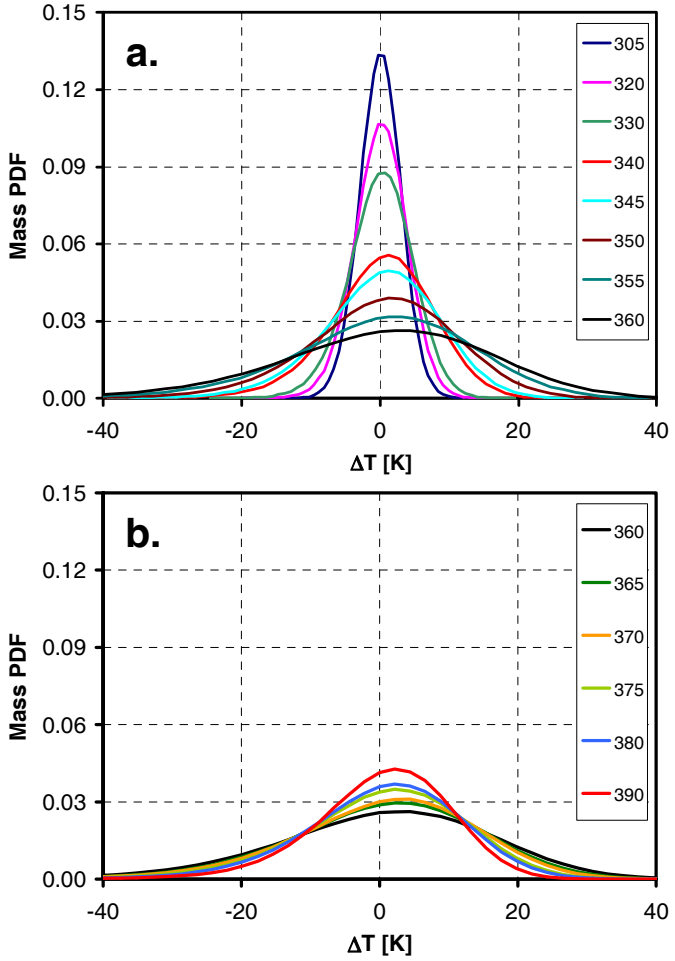

Figure 13. Ensemble-averaged, mass-weighted PDFs for 305° - 360° CA (13a) and for 360° - 390° CA (13b).

continues through 360° CA; however, after TDC the PDFs become progressively narrower again, as shown in Fig. 13b. These trends are in good agreement with the appearance of the images in Fig. 11.

As can be seen in Fig. 13, the PDFs become slightly skewed as the crank angle sequence progresses. The first PDF at 305° CA is quite symmetric, as might be expected since random measurement noise accounts for virtually all the apparent temperature variation at this crank angle (discussed above). Moving through the PDF sequence, however, the peak of the PDFs shifts to the right of the mean, and the PDFs have a longer tail on the left and drop more sharply on the right. This occurs because the real temperature fluctuations result from colder near-wall fluid being transported into a bulk gas that is initially uniformly hot. At first, this results in a distribution of colder regions over a limited portion of the charge, but there are still many high-temperature (adiabatic) regions that have not yet been affected by the colder fluid. This would result in a very skewed PDF of the real temperature distribution, but the PDFs still appear fairly symmetric because the measurement noise still contributes a very large fraction of the total PDF width. However, as time progresses, more colder fluid reaches the mid-plane, which results in two competing

effects on the skewness. First, the fractional contribution of random noise to the total PDF becomes less, increasing skewness. Second, more and more of the hot regions have some interaction with colder fluid, until there are few, if any, adiabatic regions remaining. This would cause the real-temperature portion of the PDF to become more symmetric, reducing skewness. As these two effects trade off, the amount of skewness first increases, then appears to level out with the PDF peaks remaining at about the same location for the last several PDFs shown.

To better quantify the trends in the PDF width with crank angle, the 5 – 95% TW is plotted in Fig. 14a. As can be seen, the directly measured TW increases from 10 K at 305° CA to 52 K at 360° CA. After TDC, the measured TW decreases, which will be discussed below. Based on the above analysis of noise contributions to the TW, the true TW at 305° is nearly zero, and the true TW at 360° is about 44 K. Therefore, removing the noise contribution should have the effect of shifting the curve in Fig. 14a downward by about 9 K.

Comparison of this 44 K TW at TDC with that expected from the multi-zone modeling of Sjöberg *et al.* [2] shows good agreement. Ref. [2] investigated thermal stratification using multi-zone chemical kinetic modeling to simulate experimental data acquired in an all-metal version of the optical engine used in the current study. It showed that reproducing the experimentally measured combustion PRR required a TW at BDC of 20 K, which corresponded to a TW of about 47 K at TDC for non-combusting conditions. The difference is most likely the result of the mid-plane TW = 44 K not being entirely representative of the all the bulk-gas outside the boundary layer. As will be shown in the next subsection, at TDC, a small temperature deficit (6 – 11 K) and an increase in TW is evident beginning at about half the distance from the mid-plane to the wall. This would increase the average bulk-gas stratification above the 44 K centerline value. Given the uncertainties in the TW measurements in the current study and the limitations of the multi-zone model, the agreement is considered very good.

As noted above, the TW plotted in Fig. 14a decreases after TDC. One factor contributing to this is the expansion due to piston motion. As expansion cools the charge it will proportionally decrease the TW, which is the cause of the drop in TW after TDC for the KIVA results in Fig. 10. Normalizing the data in Fig. 14a by the mean in-cylinder temperature isolates the effects of heat transfer and convection from the changes due solely to compression/expansion, as shown in Fig. 14b. With this normalization there is less decrease in the TW after TDC, but a downward trend remains. The cause of this decrease is uncertain. The most likely explanation is that there is a change in the convective transport with the reversal of the piston motion at TDC. If the downward motion of the piston significantly reduces the convective transport from the wall after TDC, the TW would progressively decrease as mixing by smaller-scale local turbulence homogenizes the existing thermal stratification.

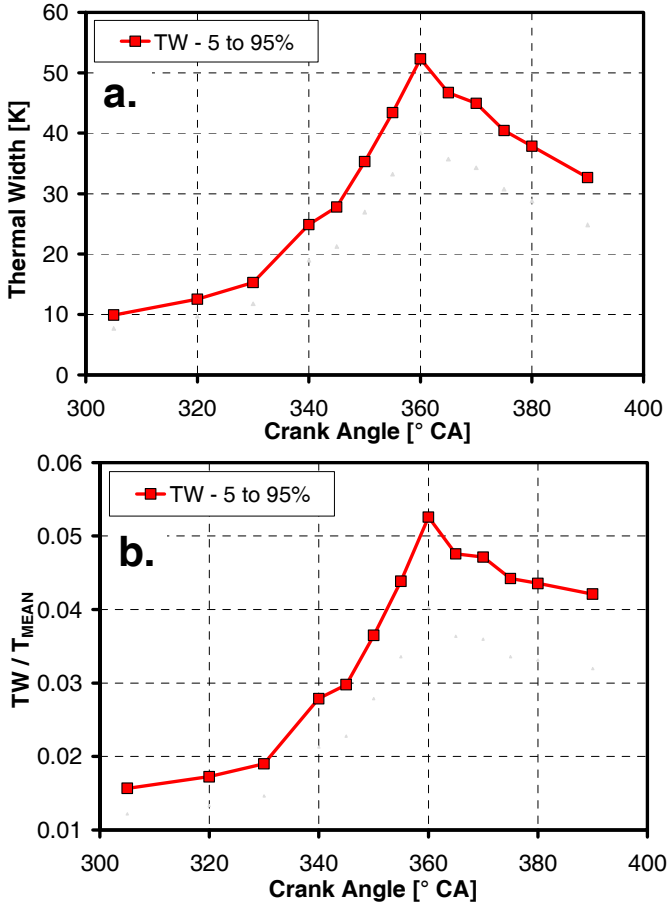

Figure 14. 5 – 95% thermal width derived from the ensemble-averaged PDFs in Fig. 13, as directly measured (14a), and normalized by the mean temperature at each crank angle (14b).

Overall, the data show a strong increase in TW by heat transfer and convection during the latter part of the compression stroke, and a relatively slower decrease in TW after TDC. In addition, the overall similarity between Figs. 14a and 14b shows that heat-transfer/convection effects dominate over the effects of compression/expansion. This point is further illustrated by the comparison of PDFs at equal crank-angle spacings before and after TDC in Fig. 15. From 330° to 390° (±30° CA from TDC), the PDF width increases greatly. Even from 340° to 380° (±20° CA from TDC) a significant increase in TW can be observed. These trends can also be observed in comparisons of the corresponding images in Fig. 11.

It should also be noted that even though the measured TW decreases somewhat after TDC for the motored engine (Fig. 14), for a fired engine, the burn duration continues to increase as the combustion phasing is retarded beyond TDC. There are several possible reasons why this occurs. First, even when hot ignition occurs after TDC, the initial autoignition reactions begin before TDC [19,20], and then, the intermediate-temperature chemistry reactions continue, progressing to hot ignition during the early part of the expansion stroke [19-21]. As a result, thermal stratification at or just before TDC still plays a role in determining the sequential autoignition timings

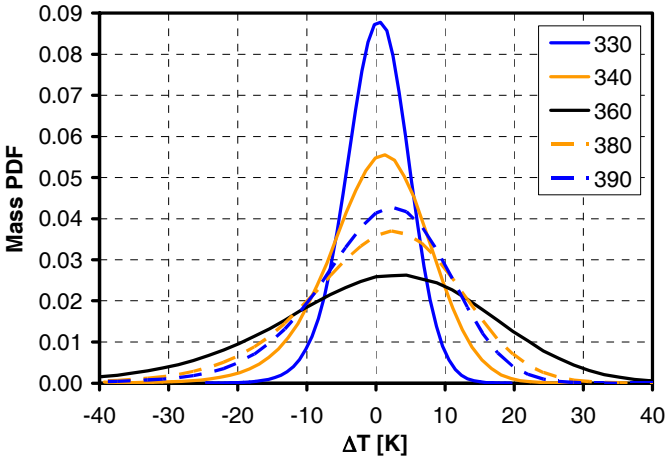

Figure 15. Comparison of PDFs at ±30° CA and ±20° CA from TDC.

of the various temperature zones. Additionally, the heat release from these intermediate-temperature reactions reduces the pressure drop after TDC, mitigating the decrease in TW compared to a motored engine. Finally and perhaps most importantly, previous work has shown that retarding the combustion phasing beyond TDC amplifies the benefit of a given thermal stratification [2]. As a result, these retarded combustion phasings have substantial benefits for slowing the heat release rate and the associated PRR with combustion [17,19] despite any decrease in the TW.

OUTER BOUNDARY-LAYER THERMAL STRATIFICATION

Although the images from the combustion-chamber mid-plane, presented above, provide a good representation of the evolution of the bulk-gas thermal stratification, it is also valuable to examine the distribution from the mid-plane to the wall. Data were acquired at two crank angles, 330° and 360° CA for laser-sheet elevations varying from the mid-plane to 0.8 mm from the firedeck. Figure 16 presents schematics showing the laser-sheet locations used for this investigation. As shown, for these data, the laser sheet was angled slightly upward to prevent interference and/or damage from back reflections. With an upward angle, the sheet is not clipped by the head prior to entering the cylinder, allowing examination of elevations closer to the firedeck. All distances are measured from firedeck downward to the laser-sheet elevation at the center of the images (see Fig. 16), in the negative "z" direction. All dimensions are normalized by "h", the firedeck to mid-plane distance, which is 9.2 mm at 330° and 4 mm at 360° as indicated in the schematic in Fig. 16. Thus, z/h = -1 is the mid-plane.

Figure 17 shows T-map image sequences at 330° and 360° CA. For both crank angles, images are presented from the mid-plane (z/h = -1) to 0.8 mm from the firedeck (z/h = -0.09 and -0.2, respectively). Similar to Fig. 11, temperatures are presented in terms of ΔT as shown in the colorbar at the bottom, and the images have been selected as being representative of sets of 40 acquired at each elevation. The corresponding temperature pro-

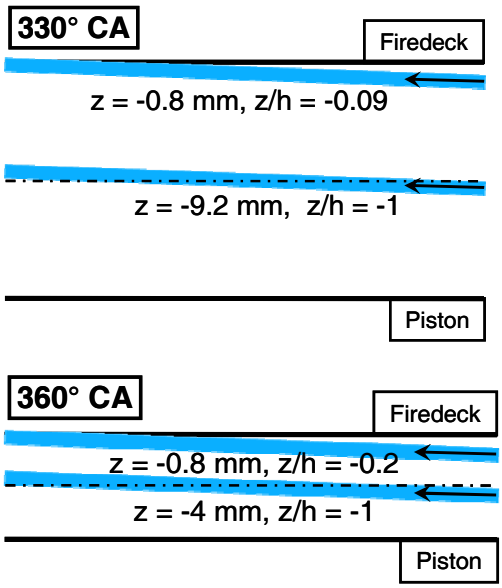

Figure 16. Laser-sheet location limits and orientation for the images in Fig. 17. The thickness of the blue line is scaled to match the approximate laser-sheet thickness. The sheet propagates from right to left.

files in Fig. 18 give the absolute temperatures averaged over the entire image and over the 40 images of each set.

At 330° CA, very little stratification appears in the mid-plane at 330° CA, as noted in Fig. 11. Moving toward the firedeck, the first significant stratification does not occur until in the z/h = -0.43 image, almost 60% of the way to the wall. Even then, the average temperature deficit is still small, as evident in Fig. 18. This large central region with little appearance of thermal stratification indicates that an intact nearly adiabatic core still exists at this crank angle. As the image plane is traversed further, to z/h = -0.22, moderate increases in the stratification and temperature deficit develop. Then, for the final two images significant stratification appears, and the temperature deficit from the mid-plane almost doubles. (These final two image planes are only 0.2 mm apart, so there is significant overlap due to the laser-sheet thickness.) It is noteworthy that for this thermal stratification, which is detected as the image plane approaches the wall ($-0.43 \leq z/h \leq -0.09$), the colder fluid appears in narrow, elongated regions, rather than in the smaller pockets seen at later crank angles in the mid-plane (Fig. 11). This shape is suggestive of vortex tubes that might be responsible for transporting this colder fluid from very near the wall to these image planes. It is also noteworthy that near the wall, the temperature distribution becomes more bimodal with large areas having temperatures well-above and well-below average.

By 360° CA, significant thermal stratification has penetrated into the mid-plane in agreement with the T-map sequence in Fig. 11. As the laser sheet traverses toward the wall, the first increase in stratification and temperature deficit are evident at z/h = -0.5. This is proportionally a little closer to the mid-plane than at 330° CA,

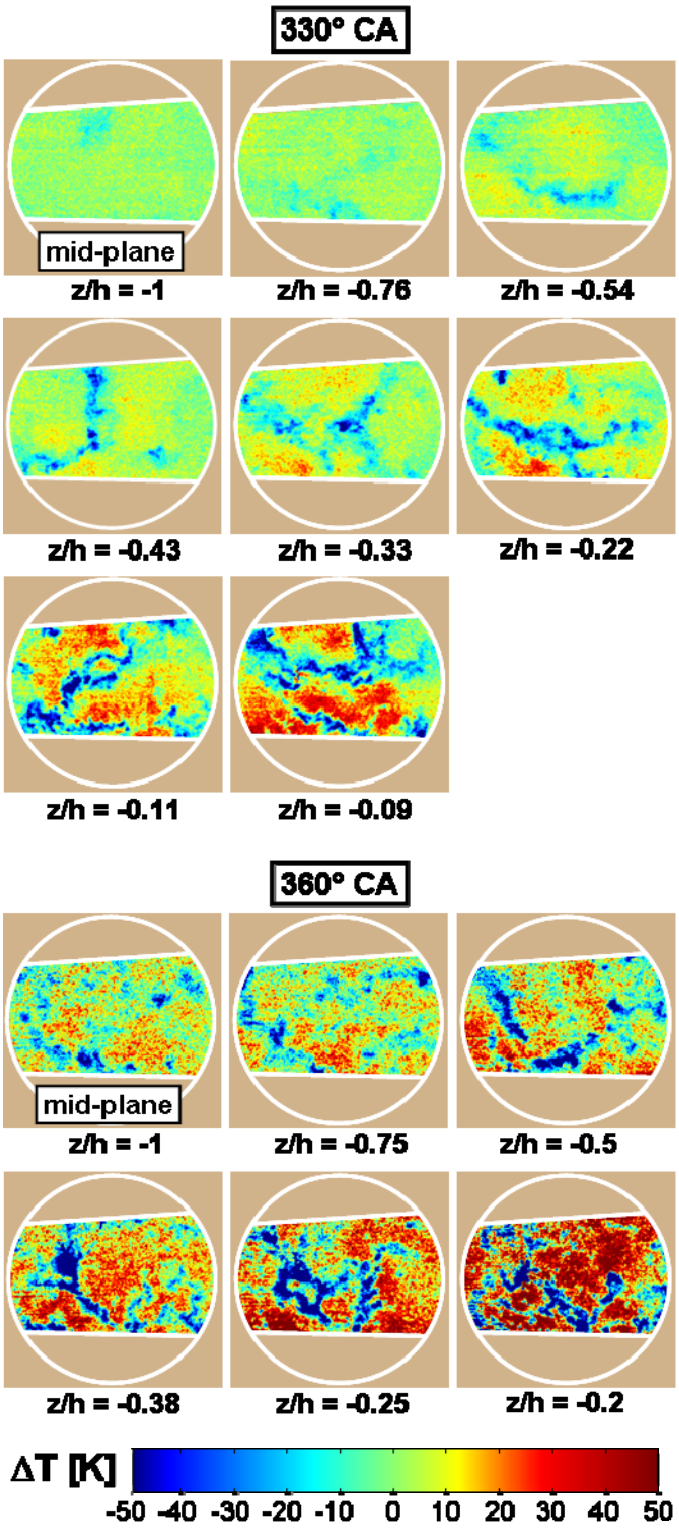

Figure 17. T-map image sequences from mid-plane to wall at 330° (top) and 360° (bottom) CA. The laser-sheet orientation is shown in Fig. 16.

where a large, nearly adiabatic core still exists. Still, the increase in stratification is not large until beyond z/h = -0.38. A substantial increase in both stratification and temperature deficit appears in the last two images. It is also evident, that with the increase in stratification for -0.5 ≤ z/h ≤ -0.2, the nature of the colder regions changes from being more pocket-like to occurring in more elongated regions that are similar to, but perhaps

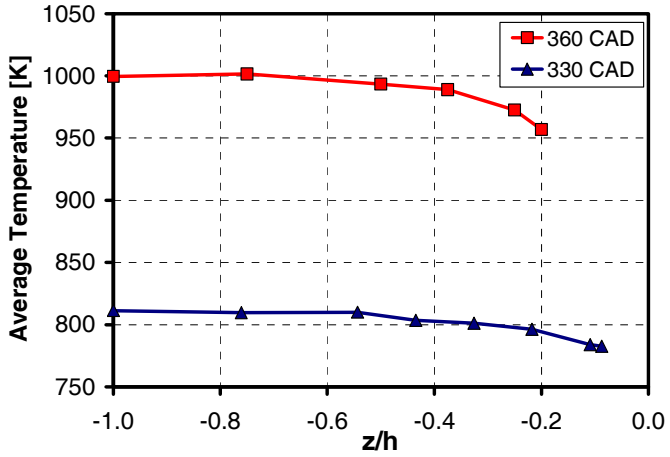

Figure 18. Averaged absolute temperatures corresponding to the selected images in the sequences in Fig. 17. z/h = -1 and 0 correspond to the mid-plane and firedeck surface, respectively. The farthest right point at both crank angles is located 0.8 mm from the surface.

not as distinct as, those in the 330° CA sequence. Also, for the two nearest-wall images, the thermal distribution appears to become even more bimodal than that of the last image in the 330° CA sequence.

Both temperature profiles in Fig. 18 are fairly flat near the mid-plane and show a decrease in mean temperature as the laser sheet approaches the wall. However, the 360° profile shows a more progressive temperature roll-off toward the wall than does the 330° profile. This indicates that the boundary layer is more developed and extends proportionally further into the charge at this later crank angle, as might be expected. Nevertheless, it should be noted that the mean temperature of both profiles must decrease to the wall value, which is about 400 K, at z/h = 0. Therefore, most of the boundary-layer temperature deficit occurs within the last 0.8 mm adjacent to the wall in both cases.

Defining a boundary-layer thickness by the location where $T-T_{wall}$ falls to 95% of its centerline value, gives a thickness of 1.5 mm (z/h = -0.16) at 330° CA and 1.0 mm (z/h = -0.25) at TDC. The thickness at TDC is in general agreement with the chemiluminescence images in Ref. [1], some of which are reproduced in Fig. 2. A detailed analysis of the chemiluminescence intensity profiles for the CR = 18 configuration of the engine used in Ref. [1] yields an estimated boundary-layer thickness of about 1 mm. A similar estimate of 1.5 mm is given by Hultqvist *et al.* [22], based on acetone-PLIF images that show the temporal and spatial distribution of fuel consumption near the wall in their CR = 10 pancake-chamber HCCI engine. The CR = 14 configuration used for the current study would be expected to give a value between these two estimates, or a little greater than 1 mm. Given the uncertainties of all these measurements, and the different boundary-layer definitions used, the agreement is considered good.

SUMMARY AND CONCLUSIONS

A planar temperature imaging diagnostic has been developed and applied to an investigation of naturally occurring thermal stratification in an HCCI engine. The temperature-map images were derived from single-line PLIF images, based on the temperature sensitivity of the PLIF signal of toluene (a trace dopant in the fuel). The diagnostic is easily implemented, but requires that the charge be well mixed. Direct measurements in the engine over a range of intake temperatures and pressures provided the necessary calibration. Although the absolute accuracy is limited by the temperatures used for calibration, which were derived from pressure measurements, the precision of the diagnostic for determining temperature variations at a given condition was shown to be very good.

Using this diagnostic, the development of the bulk-gas thermal stratification was mapped out in a motored engine from 305° – 390° CA (55° bTDC to 30° aTDC). In addition, temperature-map images were acquired from the central charge through the outer boundary layer at 330° CA and TDC. A PDF analysis of the images provided a more quantitative evaluation of the observed trends. Measurement uncertainties were evaluated and corrections applied to improve this PDF analysis. Where possible the measured thermal characteristics of the charge were compared with previous fired-engine data and modeling results, and very good agreement was found. This study produced the following specific results:

1. The single-line PLIF-based temperature imaging diagnostic works well, and produces single-shot temperature-map images with high precision. The standard deviation of precision uncertainties is 3.3 K at 305° CA and 8.8 K at TDC.

2. Initially at 305° CA, the bulk gas temperature distribution is extremely uniform. Thus, the measurements show an intact adiabatic core, and they verify that the charge is very well mixed prior to the latter compression stroke.

3. Beyond 340° CA, bulk-gas thermal stratification increases rapidly resulting in a 5 – 95% mass-based thermal width (TW) of 44 K at TDC.

4. The spatial scale of the thermal non-uniformities near TDC is 5 – 11 mm, which is comparable with the TDC clearance height of 8 mm. This scale also compares well with the size of the first bright-chemiluminescence regions for fired operation [1].

5. The spatial distribution of thermal non-uniformities shows no consistent pattern from cycle to cycle. Rather, the distributions are random, suggesting a turbulent nature to the flow structures producing them.

6. The data indicate that measured cycle-to-cycle variations in the mean bulk-gas temperature at TDC arise from a combination of small temperature variations at BDC (~37%) and variations in turbulent convection (~63%). The total measured variation closely matches the amount required to produce the typical cycle-to-cycle variations in combustion phasing for fired operation.

7. The TW decreases somewhat after TDC, due to expansion cooling and an apparent change in the in-cylinder flows. Nevertheless, the burn duration in a fired engine continues to increase with timing retard, because retard amplifies the effect of a given thermal stratification [2], and because initial combustion reactions start before TDC.

8. Measurements across the charge into the outer boundary layer show that the thermal stratification penetrates from the near-wall region at 330° CA into the entire bulk gas at TDC.

9. Moving spatially from the bulk gas to outer boundary layer at both 330° CA and TDC, the temperature spread within the images becomes greater and a bimodal distribution develops. Also, colder gases tend to occur in narrow elongated regions, rather than local pockets.

10. At TDC, the data show a 1 mm thick layer at the wall with a temperature deficit $\geq$ 27 K from the bulk gas. The thickness of this layer agrees well with the thickness derived from previous chemiluminescence imaging data [1].

Taken together, these results clearly demonstrate the dominance of wall heat transfer and convection by turbulent in-cylinder flows for producing the naturally occurring thermal stratification that is critical for high-load operation of an HCCI engine.

ACKNOWLEDGEMENTS

The authors would like to thank the following people from Sandia National Laboratories: Magnus Sjöberg for help with pressure-data analysis and for valuable discussions and Kenneth St. Hilaire, David Cicone, Gary Hux, Eldon Porter, Christopher Carlen and Gary Hubbard for their dedicated support of the HCCI engine laboratory.

This work was performed at the Combustion Research Facility, Sandia National Laboratories, Livermore, CA. Support was provided by the U.S. Department of Energy, Office of Vehicle Technologies. Sandia is a multiprogram laboratory operated by the Sandia Corporation, a Lockheed Martin Company, for the United States Department of Energy's National Nuclear Security Administration under contract DE-AC04-94AL85000.

REFERENCES

1. Dec, J. E., Hwang, W., and Sjöberg, M. (2006), “An Investigation of Thermal Stratification in HCCI Engines using Chemiluminescence Imaging,” *SAE Transactions*, 115(3) pp. 759-776, paper 2006-01-1518.

2. Sjöberg, M., Dec, J. E., and Cernansky, N. P. (2005), "The Potential of Thermal Stratification and Combustion Retard for Reducing Pressure-Rise Rates in HCCI Engines, based on Multi-Zone Modeling and Experiments," *SAE Transactions*, 114(3), pp. 236-251, paper 2005-01-0113.
3. Hultqvist A., Christensen, M., Johansson, B., Richter, M., Nygren, J., Hult, H., and Aldén, M. (2002), "The HCCI Combustion Process in a Single Cycle – High-Speed Fuel Tracer LIF and Chemiluminescence Imaging," *SAE Transactions*, 111(3), pp. 913-927, paper 2002-01-0424.
4. Sjöberg, M. and Dec, J. E. (2005), "Effects of Engine Speed, Fueling Rate, and Combustion Phasing on the Thermal Stratification Required to Limit HCCI Knocking Intensity", *SAE Transactions*, 114(3), pp. 1472-1486, paper 2005-01-2125.
5. Einecke, S., Schulz, C., Sick, V., Dreiuzler, A., Schiessl, R., and Maas, U. (1998), "Two-Dimensional Temperature Measurements in an SI Engine Using Two-Line Tracer LIF," *SAE Transactions* 107(4), pp. 1061-1069, paper 982468.
6. Fujikawa, T., Fukui, K., Hattori, Y., and Akihama, K., "2-D Temperature Measurements of Unburned Gas Mixture in an Engine by Two-line Excitation of LIF Technique," SAE paper 2006-01-3336, 2006.
7. Kakuho, A., Nagamine, M., Amenomori, Y., Urushihara, T., Itoh, T. (2006), "In-Cylinder Temperature Distribution Measurements and Its Application to HCCI Combustion," *SAE Transactions*, 115(3), pp. 648-661, paper 2006-01-1202.
8. Rothamer, D. A., Snyder, J. A., Hanson, R. K., and Steeper, R. R. (2008), "Two-Wavelength PLIF Diagnostic, for Temperature and Composition," presented at the SAE World Congress, paper 2008-01-1067, *SAE Int'l J. of Fuels and Lubricants*, in press.
9. Koban, W., Koch, J. D., Hanson, R. K., and Schulz, C. (2004), "Absorption and Fluorescence of Toluene Vapor at Elevated Temperatures," *Phys. Chem. Chem. Phys.*, 6(11), pp. 2940-2945.
10. Schulz, C. and Sick, V. (2005), "Tracer-LIF Diagnostics: Quantitative Measurement of Fuel Concentration, Temperature and Fuel/Air Ratio in Practical Combustion Systems," *Prog. Energy Comb. Sci.*, 31, pp 75-121.
11. Dec, J. E. and Sjöberg, M. (2003), "A Parametric Study of HCCI Combustion – the Sources of Emissions at Low Loads and the Effects of GDI Fuel Injection," *SAE Transactions*, 112(3), pp. 1119-1141, paper 2003-01-0752.
12. Thurber, M. C., Grisch, F., Kirby, B. J. , Votsmeier, M., and Hanson, R. K. (1998), "Measurements and Modeling of Acetone Laser-Induced Fluorescence with Implications for Temperature-Imaging Diagnostics," *Applied Optics*, 37(21), pp. 4963-4978.
13. Hwang, W., Dec, J. E., and Sjöberg, M. (2007), "Fuel Stratification for Low-Load HCCI Combustion: Performance and Fuel-PLIF Measurements, *SAE Transactions* 116(3), pp. 1437-1460, paper 2007-01-4130.
14. Sjöberg, M. and Dec, J. E., "Combined Effects of Fuel-Type and Engine Speed on Intake Temperature Requirements and Completeness of Bulk-Gas Reactions in an HCCI Engine," SAE Powertrain and Fluid Systems Conference, paper 2003-01-3173, 2003.
15. Dec, J. E. and Sjöberg, M. (2004), "Isolating the Effects of Fuel Chemistry on Combustion Phasing in an HCCI Engine and the Potential of Fuel Stratification for Ignition Control," *SAE Transactions*, 113(4), pp. 239-257, paper 2004-01-0557.
16. Sjöberg, M. and Dec, J. E. (2004), "An Investigation of the Relationship between Measured Intake Temperature, BDC Temperature, and Combustion Phasing for Premixed and DI HCCI Engines," *SAE Transactions*, 113(3), pp. 1271-1286, paper 2004-01-1900.
17. Sjöberg, M., Dec, J. E., Babajimopoulos, A., and Assanis, D. (2004), "Comparing Enhanced Natural Thermal Stratification against Retarded Combustion Phasing for Smoothing of HCCI Heat-Release Rates," *SAE Transactions*, 113(3), pp. 1557-1575, paper 2004-01-2994.
18. Sjöberg, M., Dec, J. E., and Hwang, W. (2007), "Thermodynamic and Chemical Effects of EGR and Its Constituents on HCCI Autoignition," *SAE Transactions* 116(3), pp. 271-289, paper 2007-01-0207.
19. Sjöberg, M. and Dec, J. E. (2008), "Influence of Fuel Autoignition Reactivity on the High-Load Limits of HCCI Engines," presented at the SAE World Congress, paper 2008-01-0054, *SAE Int'l J. of Engines*, in press.
20. Sjöberg, M. and Dec, J. E. (2007), "Comparing Late-cycle Autoignition Stability for Single- and Two-Stage Ignition Fuels in HCCI Engines", *Proceedings of the Combustion Institute*, 31, pp. 2895-2902.
21. Hwang, W., Dec, J. E., and Sjöberg, M. (2008), "Spectroscopic and Chemical-Kinetic Analysis of the Phases of HCCI Autoignition and Combustion for Single- and Two-Stage Ignition Fuels," *Combustion and Flame*, 154(3), pp. 387-409.
22. Hultqvist, A., Engdar, U., Johansson, B., and Klingmann, J., (2001), "Reacting Boundary Layers in a Homogeneous Charge Compression Ignition (HCCI) Engine, *SAE Transactions* 110(3), pp. 1086-1098, paper 2001-01-1032.